Achieving high strength with low residual stress in WAAM SS316L using flow-forming and heat treatment

G.G. Goviazin[1,2], D. Rittel[1], A. Shirizly[1,2]

[1] Faculty of Mechanical Engineering, Technion – Israel Institute of Technology, 32000 Haifa, Israel.

[2] Rafael, POB 2250 (774), Haifa 3102102, Israel.

- Corresponding author: Gleb Gil Goviazin gil.goviazin@gmail.com

Keywords

Wire and arc additive manufacturing (WAAM), stress relief, nano-twin, residual stress, 316L stainless steel, ring hoop tension test (RHTT), anneal hardening.

Abstract

Preformed cylinder made of wire and arc additive manufacturing (WAAM) using 316L stainless steel (SS316L) was used for a flow-forming operation to achieve a high-strength thin-walled cylinder. It was shown that the material can undergo large plastic deformation in the as-built condition without any heat treatment before the flow-forming operation. However, the flow-forming's high reduction in tube thickness and length increase generates large amounts of residual stresses that must be reduced or eliminated by appropriate heat treatment. In this work, different heat treatments on the final tube were investigated within the temperature range of 400 - 800 ℃ in air and in vacuum.

The variation in the heat treatment temperatures was observed to directly influence the residual stress values from very high initially down to almost zero at the highest temperature. It was observed on the other hand, that up to *ca.* 20 % strengthening could be gained by heat treatments up to 600 ℃, while the residual stress decreased, in comparison to the post-deformation state, as in the case of anneal-hardening. It is only past this phase that the "classical" full stress relief, with corresponding strength reduction, was achieved at 800 ℃.

1. Introduction

Additive manufacturing (AM) is a fast-growing field with many implementation techniques, part of which are powder bed fusion, direct energy deposition, binder jetting, and sheet lamination [1]. Those techniques have subclassifications such as electron beam freeform (EBF), or wire and arc additive manufacturing (WAAM) for direct energy deposition. Furthermore, additional refinement of the specific method can be done such as gas tungsten arc welding (GTAW), or gas metal arc welding (GMAW) for WAAM [2]. AM materials tend to have high residual stresses due to the rapid solidification that is inherent in most procedures, such as selective laser melting (SLM) which is part of the powder bed fusion category [3]. Hence, for engineering applications AM parts usually need to be heat treated (HTed). The Heat treatment (HT) of AM parts is not straightforward and can sometimes differ significantly from their wrought counterparts even though the same material is used [4] because of the complex thermal history in AM.

AM is a process that yields complex geometries with minimal effort and without (or with minimal) additional manufacturing processes. However, plastic deformation such as equal channel angular pressing (ECAP) can be also used to improve the material's properties [5] regardless of the final geometry. Moreover, leveraging the unique behavior of some AM materials, which present different properties compared to their wrought counterpart material [6,7], can be achieved using additional major plastic forming [8]. Both references [6,7] reported ultimate stress (UTS) of more than 1 GPa for dynamically compressed cylinders made of WAAM SS316L using Split Hopkinson Pressure Bars (Kolsky bar) apparatus [9] due to the material's unique concave up strain hardening. But the downside of severe plastic deformation is the introduction of large residual stresses which might affect any additional machining or other manufacturing processes. HT can be used to overcome this problem, once it is carefully designed to avoid loss in strength or excessive grain growth as much as possible on the one hand, and still be able to relieve the residual stresses on the other hand. While there are well-documented standards and checked procedures for wrought materials like the AMS 2759/4 standard (heat treatments for austenitic corrosion-resistant steel parts) [10], the procedures of HTs for AM materials must still be verified.

Materials strengthening by plastic deformation is caused by different microstructural changes such as the increase in the dislocation density, decrease in grain size (Hall-Petch), twining, and other effects [11]. Material's inherent properties will dictate which strengthening mechanism will be more dominant, as in the case of SS316L where deformation twinning is

the main strengthening mechanism under massive plastic deformation [12]. Moreover, nano-twins can cause even further strengthening and were reported as the main reason for the high strength achieved in bulk [13] and WAAM SS316L [7]. One should pay attention to some microstructural differences between AM and bulk materials as in the case of WAAM SS316L, which was studied by Ron et al. [14], and is identical to the one used in this work. The WAAM SS316L material is a two-phase material made of austenite grains (matrix) with a second ferritic phase located at the grain boundaries, while the bulk material is a single-phase austenite [7,14,15].

Some works concentrate on annealing and stress-relieving of as-built WAAM (and other AM) material which partially or fully softens the material [4,16–18]. However, works on strengthening by plastic deformation generally do not account for residual stress left in the material after deformation and their relief. Nevertheless, Elmer [18] rolled WAAM SS304L and then annealed it at different temperatures, first achieving high ultimate strength after rolling prior to annealing, of about 800 MPa, followed by ultimate strength decrease only after annealing at 850 ℃ and above to a value of 650 MPa and less. The work by Zhou et al. [19] can also be used for comparison of the bulk material's behavior after plastic deformation followed by annealing at different moderate temperatures. In this work a bulk SS316L reached a high ultimate strength after cold rolling, and then, the ultimate strength increased further after annealing at temperatures up to 400 ℃. Higher annealing temperatures resulted in ultimate strength decrease. According to the authors of [19], the reason for the ultimate strength increase was an increase in martensitic phase. However, for nanocrystalline nickel (Ni) Zhang et al. [20] presented increase in martensite phase with decrease in hardness, that increased only after annealing at moderate temperature of 150 ℃. The interesting anneal-hardening effect should be mentioned in this context. Here, the plastically deformed material continues to strengthen with increasing heat treatment temperatures (moderate temperatures beneath recrystallization), up to a certain point from which the material softens and the strength decreases [19,21–25]. The micromechanisms of anneal-hardening are well documented and were recently summarized in a review by Gubicza [26]. Among other mechanisms [26], the following might be relevant to this work: segregation of solute atoms to grain boundaries, twins, and dislocations which cause interaction and pinning; annihilation of defects in the grain boundaries (grain boundary relaxation) increasing their Hall-Petch hardening effect; development of "hard" texture as annihilation of mobile dislocations and rearrangement of dislocations into "hard" (clustering, pile-ups) configurations. Accordingly, the leading idea in anneal-hardening is to lower the material's energy while rearranging the

microstructure into “harder” configuration (dipolar dislocation walls, low-angle grain boundaries, etc) [25,26].

This work concentrates on the stress relief procedure for WAAM SS316L after severe plastic deformation without compromising on its high strength. The plastic deformation was carried out by flow-forming on a thick-walled cylinder and compared to wrought (bulk) SS316L. Residual stress was relieved using different HTs and the result was evaluated by comparing the achieved ultimate and residual stress results. Section 2 presents details about the specific AM procedure used, including the selected procedures for HT and the tube spinning process, experimental details, and the calculation methods for the ultimate and residual stresses. The experimental results are presented in section 3. Section 4 presents a discussion of the results followed by a conclusions section.

2. Materials and methods

2.1. Materials and specimens

WAAM (produced by GMAW) SS316L thick-walled cylinders, with 20 mm wall thickness, 95 mm inner diameter, and 120 mm height were produced in the as-built conditions. Next, preliminary machining (turning) to smoothen the surface was carried out to prepare the thick-walled cylinders for three-stage flow-forming as in [8]. The inner diameter was machined to 108.4 mm while the outer diameter was reduced from 135 to 122.5 mm, and the length was set to 110 mm, the bulk material after preliminary annealing was machined to the same dimensions. Although for industrial use a much thinner cylinder wall thickness could be built and hence achieving a much better buy to fly ratio with minimal loss (a few millimeters from each side to smoothen the surface), thicker wall thickness dimensions were chosen to be on the safe side. The final product after the flow-forming procedure was a thin-walled cylinder having 1.3 mm wall thickness, 110 mm inner diameter, and about 800 mm high (net length), thus achieving plastic strain of approximately 88% in thickness (ε_t^P) in the radial direction. The final thin-walled cylinders (both WAAM and bulk) were sliced into rings that underwent different HT procedures and were then tested for ultimate strength and residual stress evaluation. All those stages are illustrated in Figure 1.

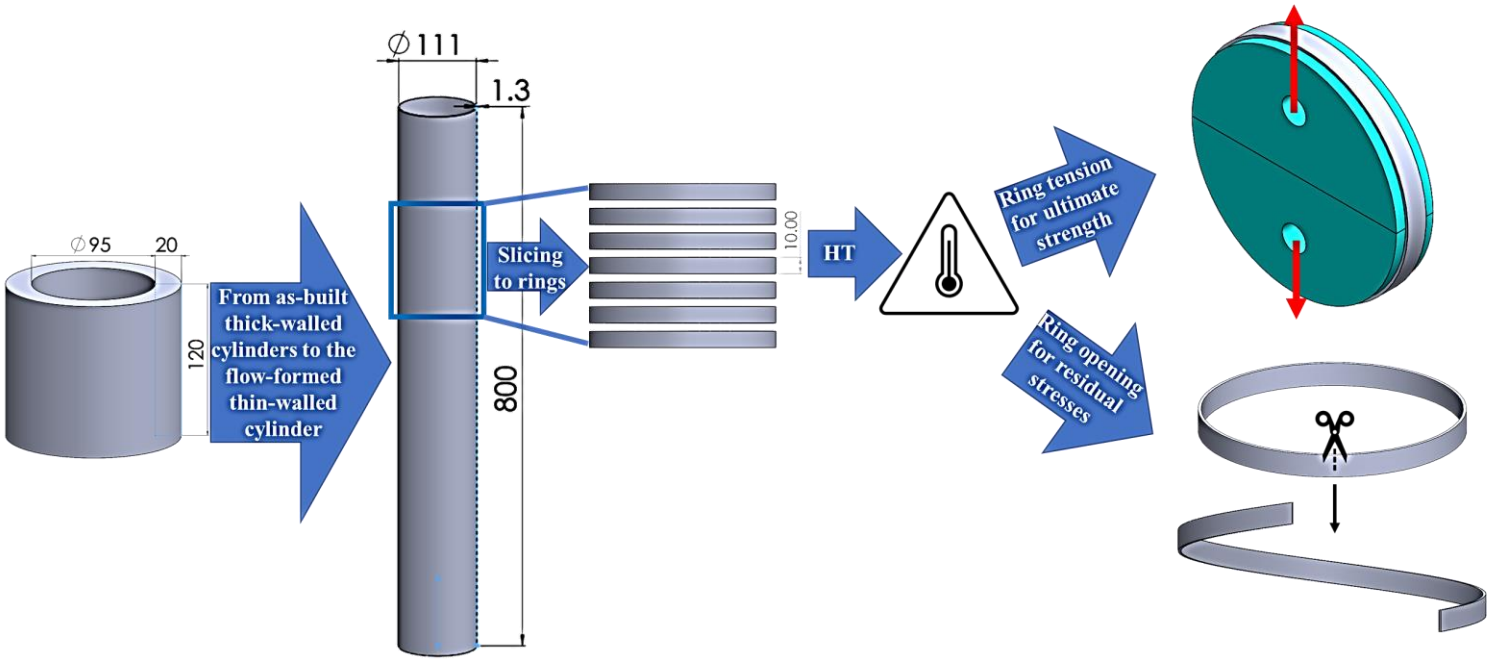

Figure 1: Stages in turning the built thick-walled cylinder to a thin-walled cylinder by flow forming, followed by cutting into rings and testing them for ultimate (ring hoop tension test) and residual stresses (slit ring).

The WAAM material of this work is identical to that of Shirizly and Dolev [8], to which the reader is referred regarding the WAAM process, flow-forming details, and other relevant parameters. One should note that the final product after forming showed a high ultimate strength of about 1.4 GPa in the tangential direction (by ring expansion), and about 1.1 GPa in the longitudinal direction (dog-bone specimen). Those high values of (anisotropic) ultimate strength are far higher than those measured on the material before deformation (about 590 MPa). However, the reason for that increase in strength was correlated to strain hardening due to plastic deformation, but the residual stresses were not relieved in their work.

2.2. Heat treatment procedures

In most cases, the material will be HTed before the flow-forming process to relieve any residual stresses. HT is important to prevent rupture while deforming, as can be seen by formability curves [27,28]. Hence, the (only) bulk material was fully annealed for 1 hour at 1060 °C in a vacuum furnace before the flow-forming process. It must be noted that the WAAM process is characterized by large surfaces, with a low ratio of surface to volume. This low ratio slows down the cooling rate of the part dramatically compared to other AM processes such as SLM. In addition, repeated thermal cycles with a slow cooling rate can be

considered to act as a “built-in annealing treatment”. Hence, it was decided to proceed with flow-forming after the WAAM process in the as-built condition without any prior HT, in contrast to the bulk material. This assumption was found to be valid since no rupture occurred while flow-forming the WAAM cylinder without prior HT. However, after severe plastic deformation (flow forming), high residual stresses could be expected and HT for residual stress relief is needed if one would require further machining of the final product (thin-walled cylinder).

According to the AMS 2759/4 standard (heat treatments for austenitic corrosion-resistant steel parts) [10], stress relief for (wrought) SS316L can be carried out at 899 ℃ while dimensional stabilization is carried out at 427 ℃. Although most stainless steels are prohibited for HT in the range of 468-816 ℃ according to this standard, SS316L (and SS304L) are permitted. To achieve sufficient stress relief while retaining the high strength of the tube after flow-forming, three temperatures were chosen in the temperature range between dimensional stabilization and stress relief, namely 400, 600, and 800 ℃. The heat treatment at each temperature was carried out once in a vacuum and once in an air furnace for the WAAM material, except for 400 ℃ which was carried out in a vacuum since it presented almost no change compared to the part with no HT. The use of both vacuum and air furnaces for the WAAM material was meant to study the material sensitivity to the surrounding environment in the HT process. The same temperatures only with an air furnace were used for the bulk materials, as summarized in Table 1. All HTs lasted one hour followed by furnace cooling. The heating rate in all cases was about 2.5 ℃/min.

Table 1: Summary of all HTs for the different materials.

Material	**Furnace**	**No HT**	**400 ℃**	**600 ℃**	**800 ℃**
Bulk	Air	✓	✓	✓	✓
WAAM	Vacuum	✓	✓	✓	✓
WAAM	Air	✓	X	✓	✓

2.3. Microstructure study

In this work we focus on the WAAM material after the flow-forming process, although for a full characterization of the material, an appendix section was added with the materials’ microstructures prior to flow-forming. The microstructure was investigated using Nikon optical microscope with up to X100 magnification, and FEI scanning electron microscope

(SEM) with Oxford INCAPentalFETx3 energy-dispersive X-ray spectroscopy (EDS). Each specimen (Table 1) was examined in all three principal directions according to a regular cylindrical coordinate system as illustrated in Figure 2. In addition, a transmission electron microscope (TEM) JEOL JEM-2100F, was used only at the largest ultimate strength points as will be discussed further. TEM examination was carried out on the WAAM material after HT at 600 ℃ and bulk material HTed at 400 ℃, both in an air furnace and in the Z direction.

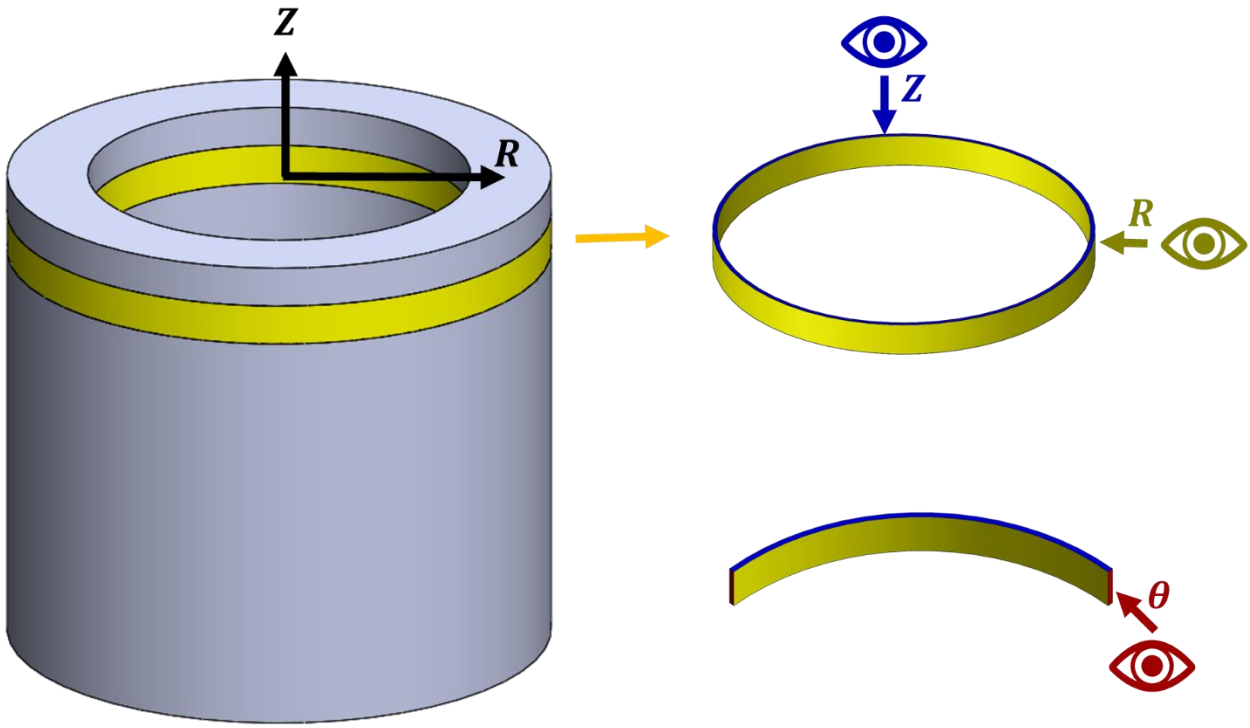

Figure 2: Specimens' principal directions as used in this study.

The chemical composition of all types of specimens was determined by optical emission spectroscopy. In addition to the usually tested metal components which SS316L is composed of, the following contaminants were tested: carbon (C), hydrogen (H), nitrogen (N), and oxygen (O). The metal components were tested using a Spectrolab™ instrument made by Spectro. The contaminants (C, H,N,O) were tested by Dirats laboratories (USA) using Leco's analyzers.

X-Ray diffraction (XRD) was carried out to shed light on the materials' (bulk and WAAM) second phase (for WAAM) and phase changes after different HTs. The bulk material was tested after deformation but prior to HT, after HT at 400 ℃ and after HT at 800 ℃,

representing the reference state, maximum UTS, and strength decrease, respectively. The WAAM material was also tested for the reference state (after deformation but prior to HT, maximum UTS (HT at 600 ℃) and after strength decreases (HT at 800 ℃). Since the WAAM material was HTed in air and vacuum furnaces, XRD was carried out at the maximum UTS point (HT at 600 ℃) for both furnaces. A SmartLab™ machine made by Rigaku with $CuK_\alpha$was used, a 2-bounce monochromator using Ge (220) crystals was added to the experimental setup to minimize fluorescence effects. Data processing was carried out in accord with the previous analysis of Ron et al. [14] who studied the same WAAM material (prior to plastic deformation). Those authors didn't observe the presence of sigma (σ) phase as observed here in accord with the study of [4]. The bulk material was analyzed in accord with the previous study of [19].

2.4. Ultimate stress evaluation

Ring hoop tension test (ring expansion) [29] was carried out to evaluate the ultimate strength (Figure 1 presents an illustration of the method). In the ring hoop tension test (RHTT) two D-blocks are pulled apart expanding the ring up to fracture, which then can be translated from the experimental force-displacement relation to stress and strain. A Shimadzu tension machine was used to pull the D-blocks apart with displacement control, which was set to 0.45 mm/min. For common practice engineering, the full ring's width is used without a reduced width (gauge) section for nominal ultimate strength calculation [8,30] according to eq. 1.

$$\sigma_{UTS} = \frac{F}{2A} = \frac{F}{2tw} \qquad eq.\ 1$$

Where σ_{UTS} is the ultimate stress, F is the applied force, $2A$ is twice the cross-section area, t is the thickness, and w is the width of the ring. Three rings were tested for each HT, and the average ultimate stress and standard deviation were calculated.

2.5. Residual stress evaluation

Residual stresses are elastic stresses stored in the material after deformation and might interfere with additional machining and final dimensions of a part as elastic springback [28]. Upon slitting the ring, a two-directional jump was observed, one in the circumferential direction (tangential – θ direction) and the other one in the longitudinal direction (RZ direction) as illustrated in Figure 3.

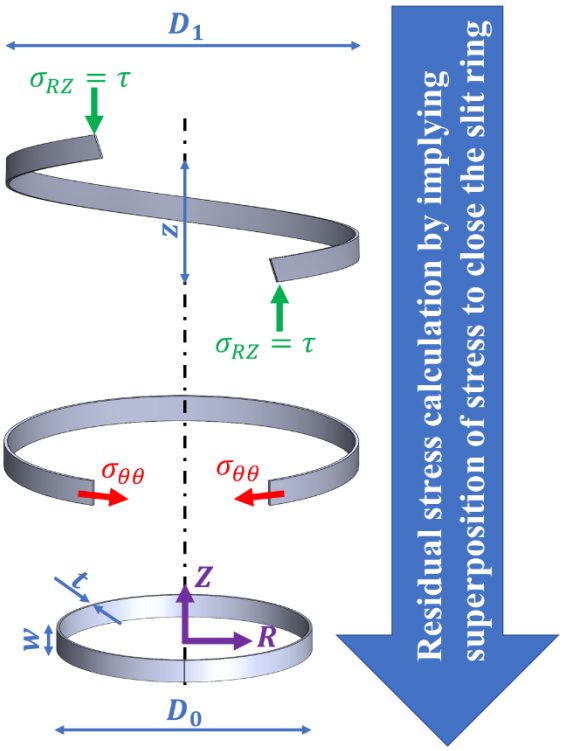

Figure 3: Illustration for the deflection of a ring upon cutting.

It should be mentioned that cutting the thin-walled cylinder into rings resulted in undeformed closed rings (prior to slitting), which implies the absence of axial residual stresses. Since the slitting releases the residual stresses responsible for the ring's deformation (jump), these can be calculated by considering the applied stresses needed to close the ring back to its original form [28]. Since the residual stresses are elastic, superposition can be used to calculate the equivalent residual stress with Von Mises' formulation. Consequently, residual stress estimation can be performed in a two-stage process as illustrated in Figure 3. That indicates that first the shear stress ($\sigma_{RZ} = \tau$) can be calculated by bringing the corresponding slit planes to coincide into one plane, and then the circumferential stress ($\sigma_{\theta\theta}$) can be calculated by closing the ring upon itself. Note that all the other stress components are zero which implies the simplification presented in eq. 2.

$$\sigma_e = \sqrt{\frac{1}{2}\left[(\sigma_{RR} - \sigma_{zz})^2 + (\sigma_{RR} - \sigma_{\theta\theta})^2 + (\sigma_{\theta\theta} - \sigma_{zz})^2 + 6\left(\sigma_{RZ}^2 + \sigma_{R\theta}^2 + \sigma_{Z\theta}^2\right)\right]} \quad \text{eq. 2}$$

$$= \sqrt{\sigma_{\theta\theta}^2 + 3\sigma_{RZ}^2} = \sqrt{\sigma_{\theta\theta}^2 + 3\tau^2}$$

Among the methods for circumferential residual stresses evaluation ($\sigma_{\theta\theta}$), the deflection method for thin-walled cylinders was chosen due to its relative simplicity and is presented in eq. 3 [28].

$$\sigma_{\theta\theta} = \frac{E}{1-\nu^2}\left(\frac{1}{D_0} - \frac{1}{D_1}\right) \quad \text{eq. 3}$$

When $E = 193\ GPa$ and $\nu = 0.27$ are the material Young's modulus and Poisson's ratio, respectively. D_0 and D_1 are the diameters of the ring before and after opening (as if it was closed while $D_0 < D_1$) it, respectively (Figure 3).

The shear stress ($\sigma_{RZ} = \tau$), caused by the vertical deflection, was calculated by using spring's formulation due to the kinematics of the spring-like slice in eq. 4 [31].

$$\tau = \frac{FD_0(3t + 1.8w)}{2t^2w^2}\left(1 + \frac{1.2}{c} + \frac{0.56}{c^2} + \frac{0.5}{c^3}\right) \quad \text{eq. 4}$$

Where $c = D_0/t$ and F is the required force to bring the spring (ring) into the required position. In this case, F is the required force to bring the ring back to one flat plane (Figure 3) and can be calculated by eq. 5 [31].

$$F = \frac{4zGt^4}{3\pi D_0^3 n}\left\{\frac{w}{t} - 0.627\left[\tanh\left(\frac{\pi t}{2w}\right) + 0.004\right]\right\} \quad \text{eq. 5}$$

Where z is the total measured movement (jump) of the ring in the Z direction, $G = 78\ GPa$ is the shear modulus, n=1 is the number of active loops in the spring (the ring is like a single loop spring).

Substituting eq. 3 and eq. 4 into eq. 2 yields eq. 6 which was used to evaluate the equivalent residual stresses in the different rings. Three rings were tested for each HT, and the average residual stress and standard deviation were calculated.

$$\sigma_e = \sqrt{\sigma_\theta^2 + 3\tau^2}$$
$$= \sqrt{\left[\frac{E}{1-\nu^2}\left(\frac{1}{D_0} - \frac{1}{D_1}\right)\right]^2 + 3\left[\frac{FD_0(3t + 1.8w)}{2t^2w^2}\left(1 + \frac{1.2}{c} + \frac{0.56}{c^2} + \frac{0.5}{c^3}\right)\right]^2} \quad \text{eq. 6}$$

3. Results

3.1. Ultimate and residual stresses

As stated before, WAAM and bulk materials were tested for ultimate and residual stresses after a variety of HTs, using three rings per test at each HT and for each material. A summary of the results is presented in Figure 4 for the average ultimate stress (solid line) of each test

with its residual stress values (dashed line in the same color). The vertical lines representing the extreme values are sometimes shorter than the markers representing the measured points, due to the small differences that were measured between tests.

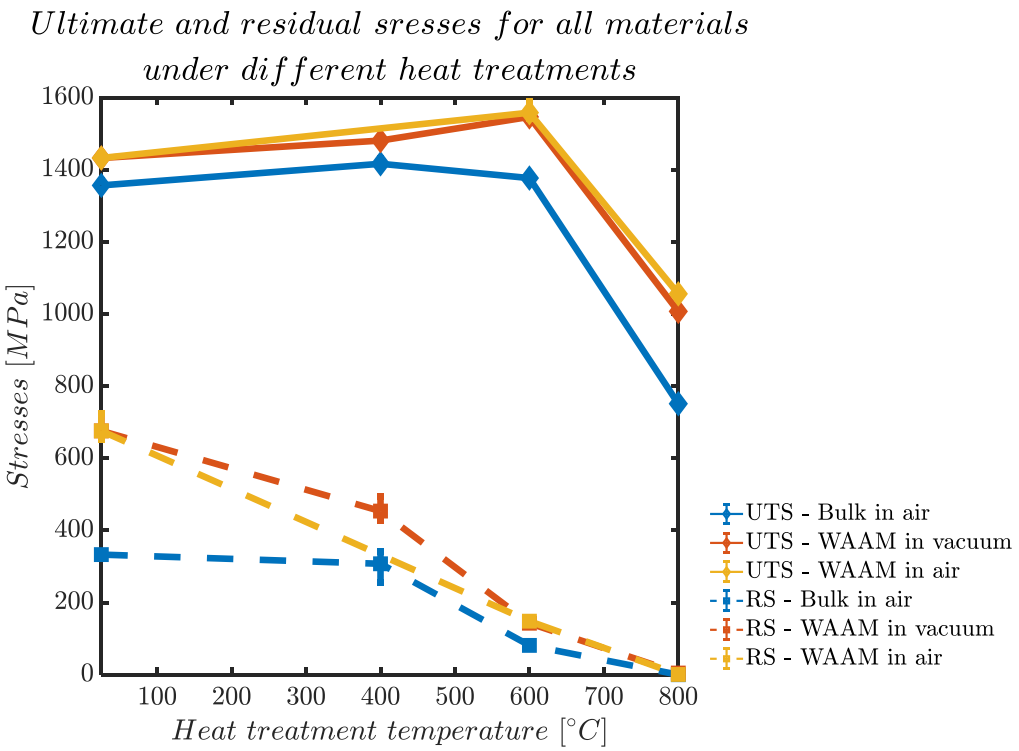

Figure 4: Ultimate strength (UTS) and residual stress (RS) results for different HTs. The lines are linearly interpolated between measured points (markers). Extreme values are represented by the vertical line, which is sometimes less than the marker size.

The WAAM material showed a similar behavior at each HT temperature for both ultimate and residual stresses, regardless of the furnace's environment. Namely, it presented a rise in the ultimate stress up to the maximum ultimate stress achieved after HT at 600 ℃ followed by a decrease at 800 ℃. By contrast, the residual stress was observed to monotonically decrease with HT temperature. A similar behavior was observed for the bulk material, but the maximum ultimate stress was observed for HT at 400 ℃. The ultimate stresses of the WAAM material exceed those of the bulk material for all HTs, reaching about 1560 MPa (at 600 ℃) for the WAAM material as compared to about 1420 MPa for the bulk material. On the other hand, the residual stresses of the WAAM material exceed those of the bulk material, but the difference between them becomes much smaller at higher HT temperatures, hence presenting much larger residual stresses at 400 ℃ compared to 600 ℃. The importance of the residual stress relief after vacuum HT of the WAAM material, is illustrated in Figure 5.

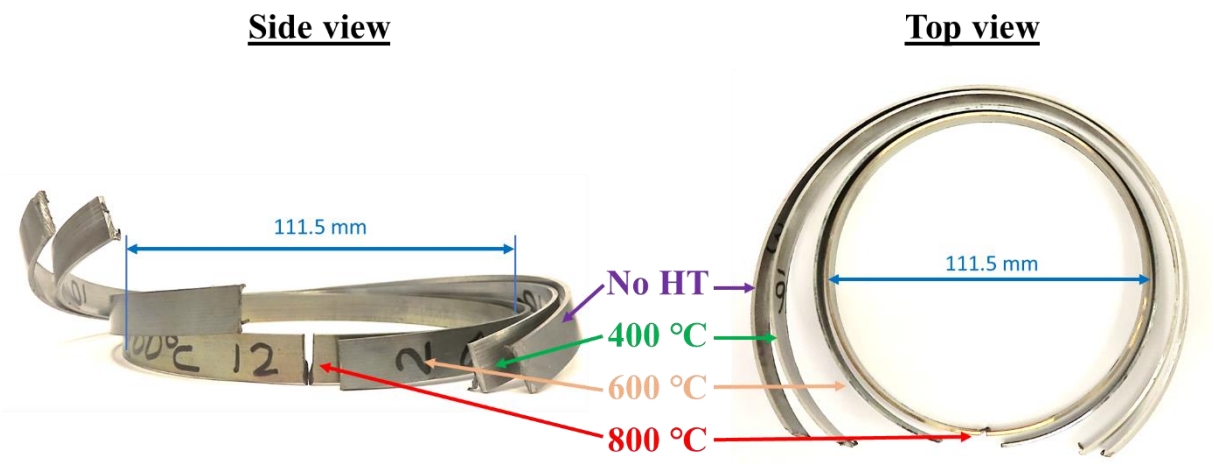

Figure 5: Representative pictures of rings' deflection after opening (caused by stress relief). The specific rings are made of WAAM and HT in a vacuum furnace.

As mentioned, the WAAM material was treated in both vacuum and air furnaces, except for the HT in the air furnace at 400 ℃. This last HT was neglected due to the small effect in ultimate stress seen for the vacuum furnace test at the same temperature (400 ℃), and the generally good agreement in ultimate and residual stresses for WAAM both in air and vacuum HTs.

3.2. Microstructure

A preliminary visual inspection was carried out, revealing that 600 ℃ and 800 ℃ ring HTed in an air furnace, for both WAAM and bulk materials, caused surface oxidation. On the other hand, the rings HTed in a vacuum didn't present any visual surface oxidation as shown in Figure 6.

Figure 6: Rings made of both WAAM and bulk materials after HT at 800 ℃, the WAAM was HTed in a vacuum and air furnace while the bulk was only in an air furnace. Presenting surface oxidation for the rings HTed in air furnace (both WAAM and bulk) in contrast to the one HTed in vacuum furnace (WAAM).

The chemical composition of the rings was determined to evaluate the percentage of oxygen and other contaminants which might influence the results. As presented in Table 2, chromium (Cr) percentage was higher than standard for the WAAM material, while sulfur (S) was higher than the standard for the bulk material (for all heat treatments). In addition, it can be seen that bulk material treated above 400 ℃ causes oxygen and nitrogen absorption. No such behavior was observed for the WAAM material. However, the highest oxygen and nitrogen values found in the bulk material are identical to the ones present in the as-built WAAM material (prior to flow-forming). The nitrogen in all cases was within the permitted limit, while there is no such limit on oxygen. Surprisingly, the oxygen and nitrogen values decreased in the WAAM material after heat treatment in air. Although only one specimen was tested for each HT (each line in Table 2), so that the standard deviation cannot be reported, there is a good agreement between both WAAM specimens HTed in air, i.e., the Air 600 ℃ and Air 800 ℃ WAAM specimens.

Table 2: Chemical composition of the rings determined by optical emission spectroscopy.

	Heat treatment (HT)	**chemical composition, wt. %**											
		C	**Si**	**Mn**	**P**	**S**	**Cr**	**Ni**	**Mo**	**N**	**O**	**H**	**Fe**
WAAM	As-built - No HT (prior to flow-forming)	0.011	0.46	1.86	0.019	0.001	18.3	11.8	2.58	0.061	0.035	0.001	64.8
	No HT (after flow-forming)	0.012	0.46	1.85	0.02	0.001	18.2	11.8	2.6	0.062	0.034	0.001	64.7
	Vaccum 400 ℃	0.012	0.46	1.85	0.022	0.001	18.2	11.8	2.6	0.062	0.033	0.001	64.7
	Vaccum 600 ℃	0.011	0.45	1.87	0.019	0.001	18.1	11.8	2.61	0.062	0.037	0.001	64.8
	Vaccum 800 ℃	0.012	0.46	1.89	0.02	0.001	18.2	11.8	2.6	0.062	0.038	0.001	64.7
	Air 600 ℃	0.014	0.45	1.87	0.019	0.002	18.1	11.8	2.6	0.039	0.005	0.001	64.8
	Air 800 ℃	0.015	0.46	1.9	0.02	<0.001	18.1	11.8	2.61	0.039	0.005	0.001	64.8
Bulk	No HT (after flow-forming)	0.015	0.56	1.82	0.018	0.033	16.7	11.2	2.07	0.038	0.004	0.001	67.1
	Air 400 ℃	0.013	0.57	1.8	0.024	0.04	16.8	11.3	2.01	0.041	0.004	0.001	67
	Air 600 ℃	0.011	0.58	1.87	0.025	0.044	16.7	11.5	2.05	0.063	0.036	0.001	66.7
	Air 800 ℃	0.017	0.57	1.81	0.022	0.043	16.6	11.3	2.07	0.063	0.036	0.001	67.2
ASTM A240 / 240M - 316L		Max 0.030	Max 1.000	Max 2.000	Max 0.045	Max 0.030	16.00-18.00	10.00-14.00	2.00-3.00	Max 0.100	-	-	-

Optical and SEM microscopy was carried out for each HT and material, and all rings' principal directions (Figure 2) were inspected. The specimens were etched using 20 ml of HNO_3, 45 ml of HCl, and 25 ml of ethanol. For clarity, and without loss of generality, only representative cases are presented in the sequel.

The optical microscopy revealed largely deformed microstructures for all materials (WAAM and bulk for all HTs) due to the massive plastic deformation of the material. The flow-forming process was done with a 0.7mm pitch, resulting in a periodic pattern found for all specimens and all HTs in the R direction (marked with yellow arrows in Figure 7). In addition, the θ and Z directions presented layered-like patterns, with some waviness in the θ direction that were better seen for the bulk material. Representative pictures are presented in Figure 7 for HT at 600 ℃.

	R direction	**θ direction**	**Z direction**
Bulk – HT in air @ 600 ℃	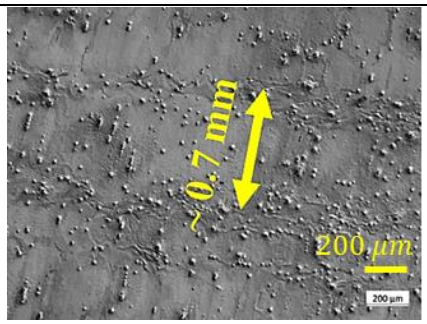	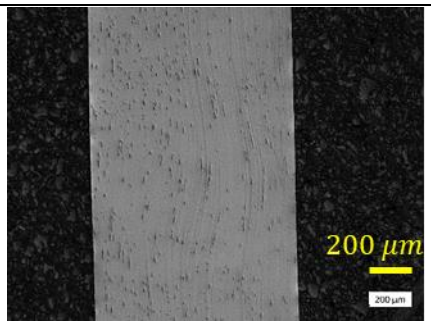	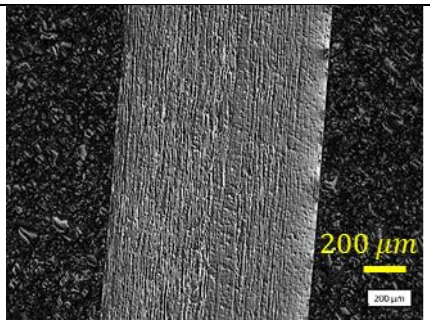
	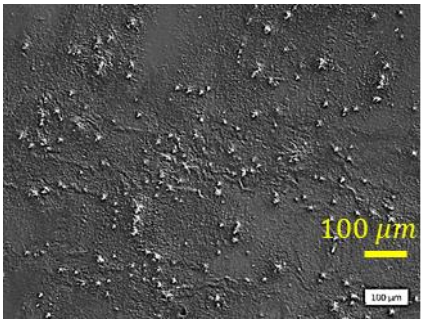	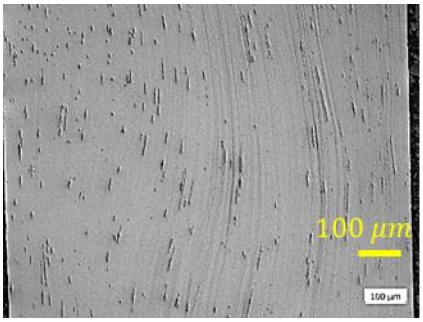	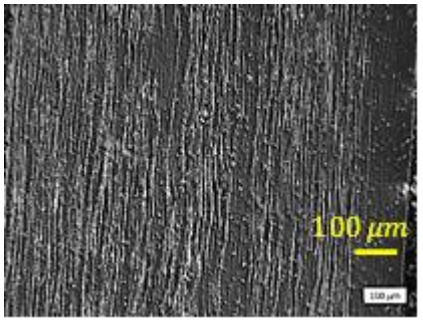
WAAM – HT in vacuum @ 600 ℃	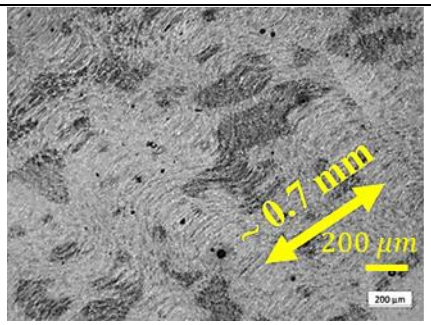	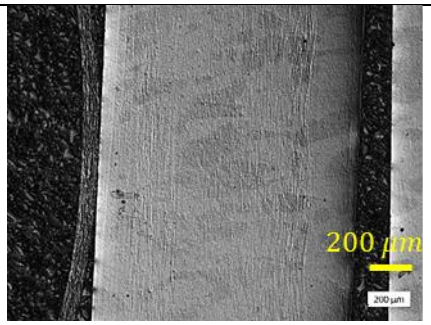	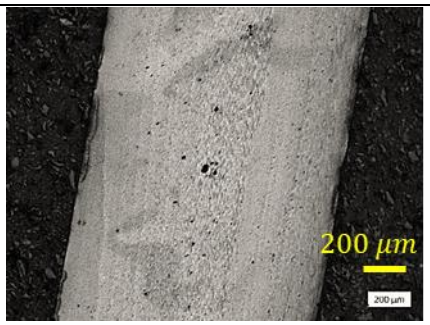
	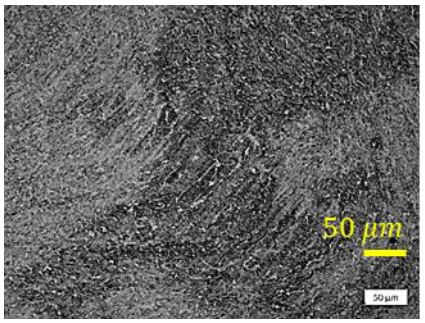	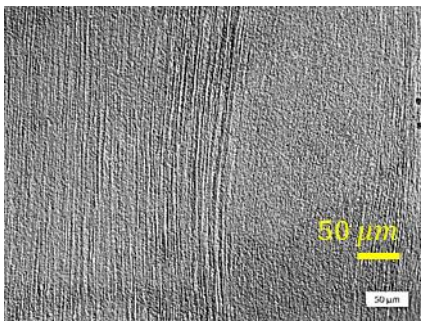	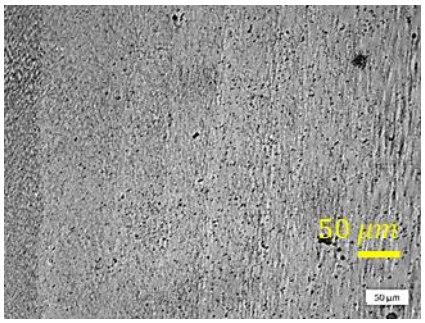

WAAM – HT in air @ 600 °C	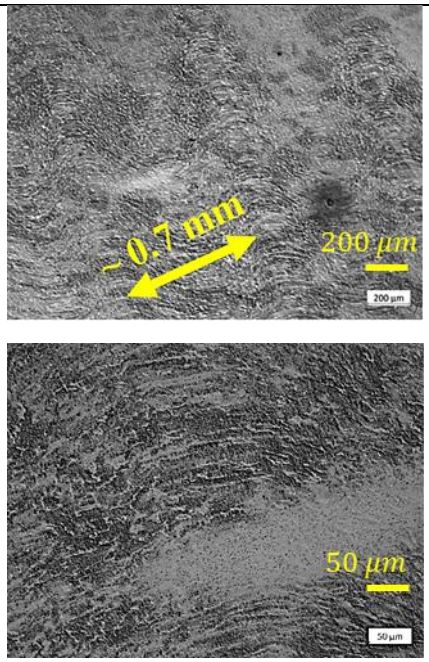	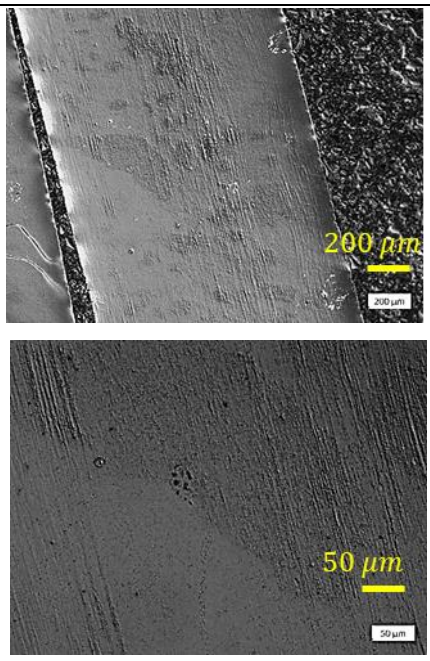	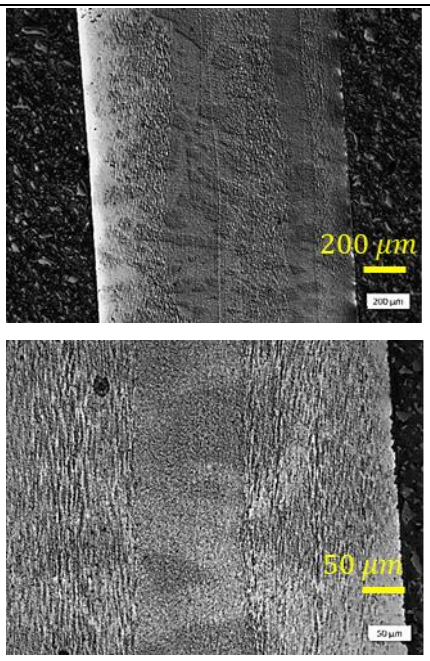
Pattern summary	Periodic behavior with similar spacing to the process' pitch	Layered like structure with some curviness	Linearly layered like structure

Figure 7: Representative optical microscopy pictures of WAAM and bulk specimen HTed at 600 °C in air (WAAM and bulk) and vacuum (WAAM) furnace, presenting largely deformed microstructure. The directions indicate the planes' normal directions as specified in Figure 2. The arrows in all R direction pictures present repeatability in the microstructure which was identical to the flow-forming pitch of 0.7 mm.

SEM examination did not reveal additional information, except that as the HT temperature increased, so did the oxygen-rich regions as was verified by EDS (*Figure 8*). This corresponds to the corrosion detected at the elevated temperatures (Figure 6).

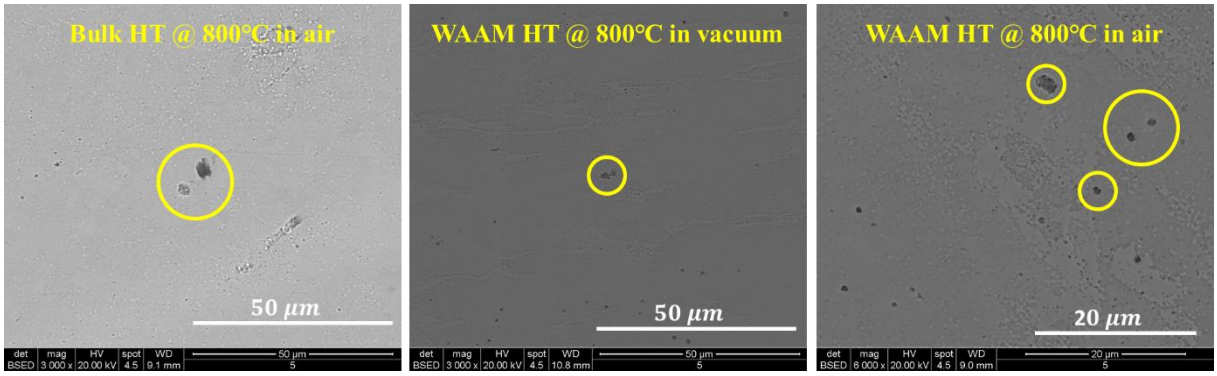

Figure 8: SEM pictures presenting oxygen-rich regions as verified by EDS. Note the different magnifications.

Further investigation of the materials to understand the reason for the materials' strengthening was carried out by TEM. Only two samples were taken, so it was decided to investigate the maximum ultimate stress points. Hence, one sample was taken from the WAAM material in the R direction after HT at 600 ℃, and the other one was taken from the bulk material in the R direction after HT at 400 ℃. To maintain some similarity both specimens were taken from materials after HT in an air furnace. Although both materials presented nano-twins, those had different characteristics. While the WAAM material presented short spacing (10-50 nm) between nano-twins, the bulk material presented larger spacing between nano-twins (more than 60 nm) which were hard to observe at high magnification observations. Shorter spacing between nano-twins implies higher material's strength. Both cases are presented in Figure 9.

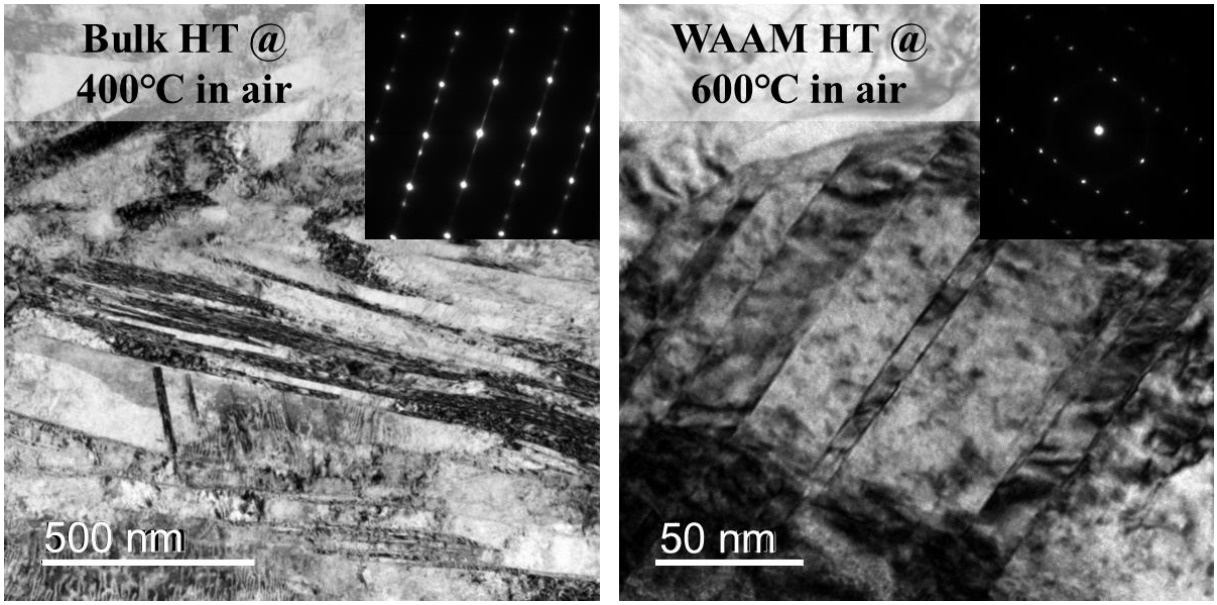

Figure 9: TEM pictures at the maximum ultimate stress points for bulk (400 ℃) and WAAM (600 ℃) materials, both HTs in an air furnace. Both pictures and inserts present nano-twins. Pay attention to the different magnifications due to different nano-twins' lengths.

The XRD presented a single ferrite phase for the bulk material after deformation for all HTs, with peaks shift toward higher angles after HT at the 800 ℃. On the other hand, the WAAM material presented a two phase material (austenite and ferrite) for all samples, also presenting some peaks shift for the austenitic phase at elevated HT. However, the ferritic phase which was clearly present at HTs up to 600 ℃ almost disappeared at 800 ℃, where a σ phase started to appear, as presented in Figure 10.

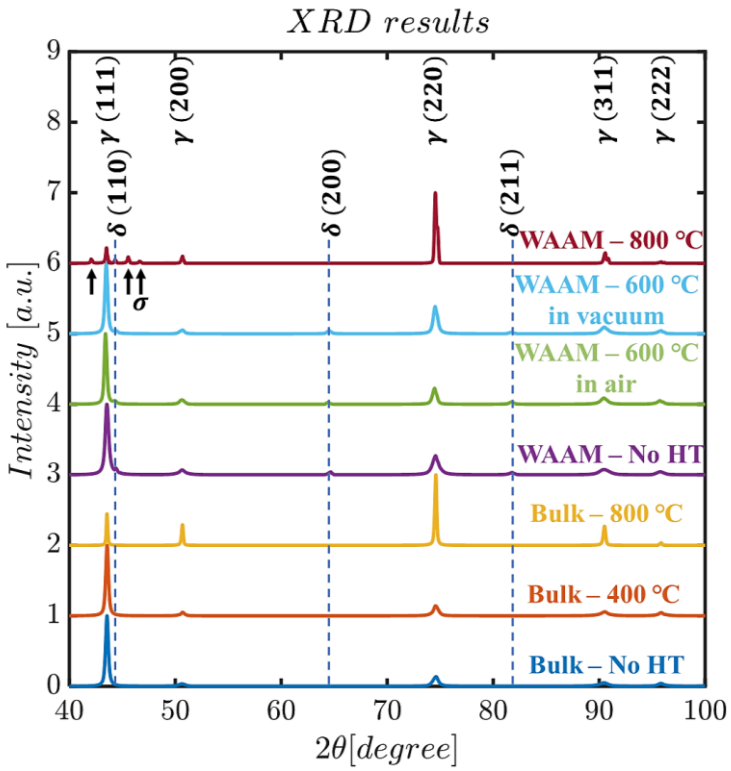

Figure 10: XRD results for bulk and WAAM materials after flow forming and for different HTs, as written next to each curve. Each peak is described by the γ-austenite or δ-ferrite (also dashed vertical lines) description at the top. The arrows pointing to the WAAM – 800 °C curve indicate σ phase peaks.

4. Discussion

It was observed that very high strength levels could be achieved from bulk and WAAM SS316L materials after massive plastic deformation using flow-forming, at the cost of significant residual stresses. The initial differences in the residual stresses after flow forming and prior to any HT between the bulk and WAAM materials are probably due to the initial difference in microstructure (WAAM had smaller grains) and the thermal conditions of the materials. The bulk material was fully annealed prior to flow forming while the WAAM was used in the as-built condition, and hence probably had some small amount of residual stresses from the building process itself (prior to flow-forming). Considering the as-built WAAM material as an annealed-like material was found to be a good approximation as evidenced by its ability to withstand large plastic deformations. The post flow-forming residual stresses were relieved using a variety of heat treatments. The "classical" expected response of steel subjected to HT is simultaneous strength and residual stress reduction as the HT's temperature is higher, when in parallel, strengthening can be a side effect of high residual stress. However, we observed here that although the residual stress decreases significantly,

the ultimate strength increases with temperature. This increase in ultimate stress was up to the temperature of 400 ℃ for bulk and 600 ℃ for WAAM materials, respectively. Beyond those temperatures, a decrease in both ultimate and residual stresses was observed, as one would expect from the "classical" behavior. Similar results were obtained by Elmer [18] for WAAM SS304L and Zhou et al. [19] for bulk SS316L materials as presented earlier. From a practical point of view, HT of WAAM SS316L at 600 ℃ in vacuum yielded the best performance in this work, namely the highest ultimate stress (1560 MPa) with almost negligible residual stress (150 MPa), and without any evidence of corrosion signs. This is a clear indication that residual stresses do not influence this material's strength, although such stresses are not desirable in general.

The XRD analyzes presented austenitic peaks' shift to higher angles for HTs at 800 ℃ for both bulk and WAAM materials, which indicates a change in the micro-strain state [4]. The change in the strain state was also presented macroscopically (Figure 4) by zero level residual stresses for the HT at 800 ℃. Although Zhou [19] found a martensitic phase in bulk SS316L after rolling, no second phase was found in the bulk material herein, having only austenite phase. The WAAM material presented both austenite and ferrite phase up to HT at 600 ℃, transferring the ferrite phase into a sigma (σ) phase at 800 ℃ as was previously reported for this material by Rodrigues et al. [4] who tested it at 950 ℃. Rodrigues et al. [4] also presented a decrease in hardness for this temperature which can be correlated to decrease in stress as presented in this work. An important remark should be made regarding the maximum UTS points of both bulk (after HT at 400 ℃) and WAAM (after HT at 600 ℃) materials, where no phase transition or peaks shift occurred as compared to prior HT regardless of the increase in UTS. This fact of no phase transition at the UTS (400 ℃ for the bulk and 600 ℃ for the WAAM materials), combined with the rise in UTS after HT at moderate temperature of plastically deformed materials, and the decrease thereafter at higher temperatures, points to the anneal-hardening effect as the probable reason for the UTS increase.

Since the emphasis of this work was the macroscopic behavior of the materials (macroscopic ultimate and residual stresses), the microstructure investigation carried out in this work was meant for a preliminary comparison with previously reported results. A thorough microstructural investigation is out of the scope of this work but is definitely a point to be elucidated if one wants to better understand the physical mechanism behind the identified optimal temperature for the heat treatment of WAAM SS316L. Microstructural characterization at the nanoscale revealed a profusion of nano twins which were formed

during the plastic deformation and probably evolved during HT (combined with the effect of anneal-hardening). The achieved TEM and mechanical trends of the bulk material's nano-twins and ultimate strength resemble those reported in [12,19] while the WAAM materials' response resembles that reported in [7]. From the microstructural investigation, the following comparison between bulk and WAAM materials can be made. First, both microstructures comprise nano-twins of somewhat different spacing, leading to a different level of local strain hardening. In addition, the fact that the WAAM steel is a two-phase material (austenite and ferrite) might enhance different microstructural changes (compared to bulk material) leading to low energy hard configurations, and hence anneal-hardening effect with additional mechanisms. Finally, difference in the initial grain sizes (~10 μm in WAAM compared to ~60 μm in bulk, see appendix section) and thermal conditions (annealed bulk as opposed to as-built WAAM) might explain the somewhat different mechanical properties between the WAAM and bulk materials.

Finally, the chemical composition study showed that the initial levels of oxygen and nitrogen in the WAAM material were similar to those of the bulk material only for HTs in air atmosphere above 400 ℃. Comparing those results to those of Elmer and Gibbs [32], the oxygen absorption could be caused the WAAM building process which was carried out in air atmosphere (no in inert environment), or even by the 2 % oxygen addition (for oxygen addition, nitrogen from atmosphere) that was added to the shielding gas of the welding torch.

5. Conclusions

Flow-forming of a WAAM SS316L cylinder, followed by heat treating at 600 ℃ (preferably in vacuum), yields an ultimate stress of 1560 MPa and with almost no residual stress in the final product. Further increase of the HT temperature beyond 600 ℃, while further reducing the residual stresses, causes a reduction in strength as would be expected in a "classical" HT. Having ruled out residual stresses and as a strengthening factors, and after conducting a variety of examinations which reveal microstructural changes such as nano-twinning, which combined with anneal-hardening (no phase transition), might be the reasons for the high ultimate stresses achieved. However, the microstructural changes must be further examined to pinpoint the evolution of the nano-twins and the manifestation(s) of the exact mechanism of anneal-hardening for this material.

6. Appendix

6.1. Appendix A – microstructure prior to flow-forming

Although this work concentrated on the Bulk and WAAM materials' properties after deformation, the microstructure prior to flow forming is presented in Figure A 1. The annealed bulk material presented grain size of about 60 μm while the as-built WAAM materials had grain size on the order of 10 μm. For a more thorough investigation of the same as-built WAAM material's microstructure the reader is kindly referred to the work of Ron et al. [14].

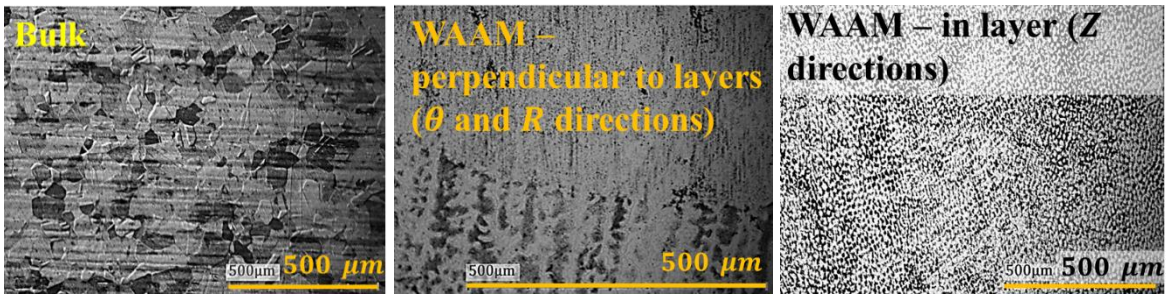

Figure A 1: Microstructure of bulk and WAAM materials prior to flow-forming

6.2. Appendix B – rings microstructure in all principal directions and heat treatments

All microstructures, of both materials and heat treatments, are presented below for a full picture presentation. WAAM without heat treatment is of course identical for both Table A. 2 and Table A. 3.

Bulk material in air furnace

	***R* direction**	***θ* direction**	***Z* direction**
Bulk – No HT	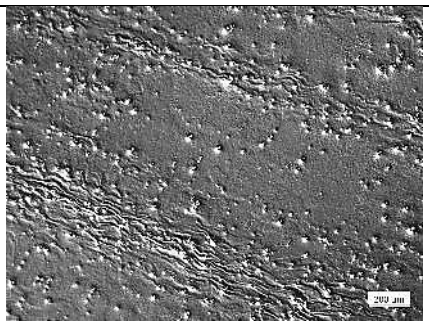	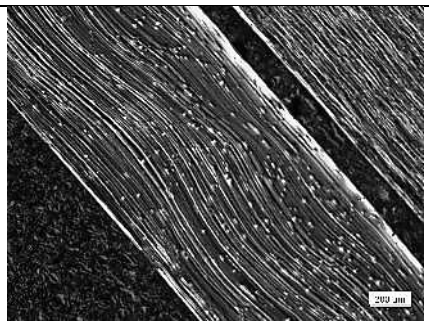	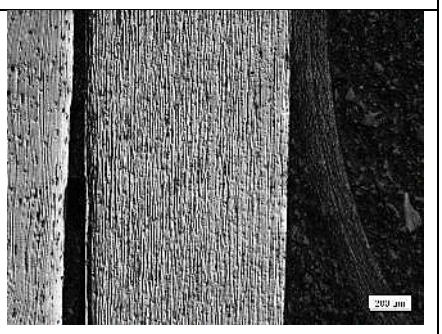

Bulk – HT in air @ 400 °C	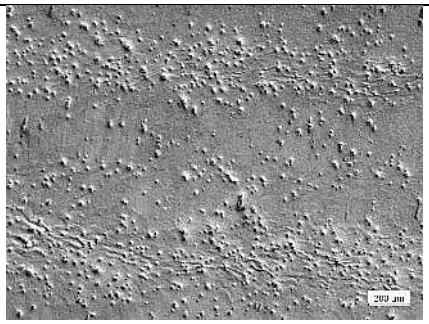	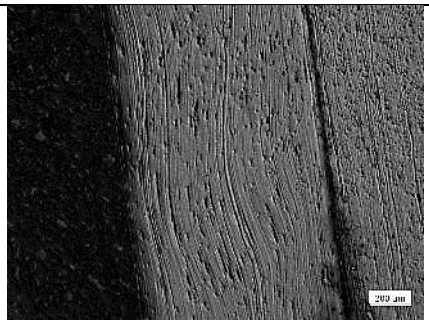	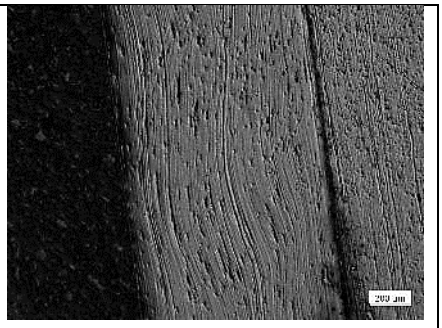
Bulk – HT in air @ 600 °C	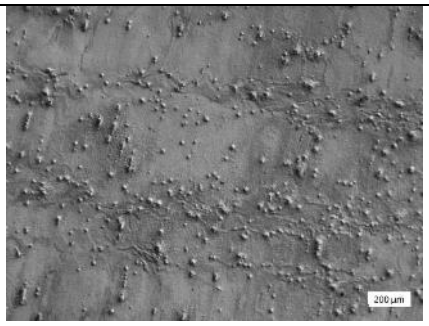	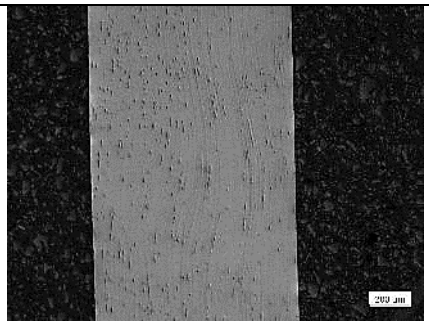	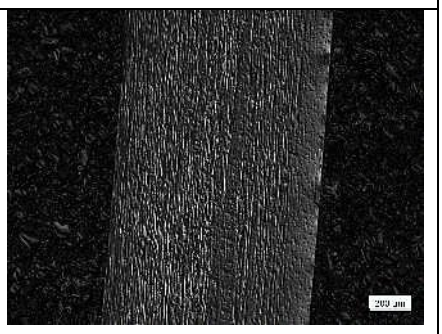
Bulk – HT in air @ 800 °C	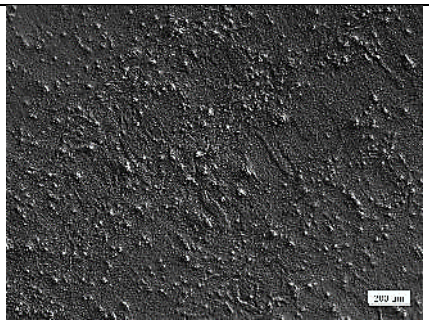	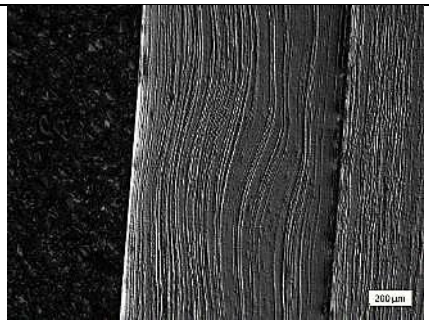	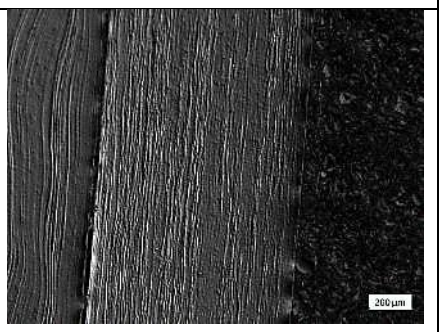

Table A. 1: Microstructure of bulk material heat treated in air furnace, presented in all three principal directions. All pictures have the same magnification, the white box width is 200 μm.

<u>WAAM material in air furnace</u>

	***R* direction**	***θ* direction**	***Z* direction**
WAAM – No HT	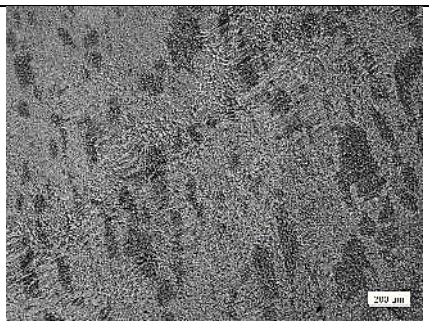	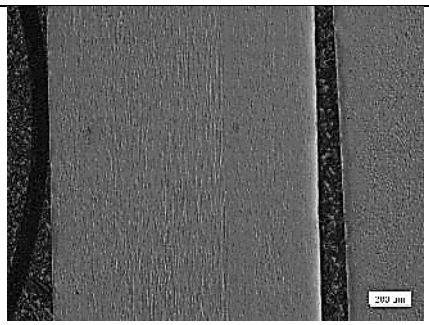	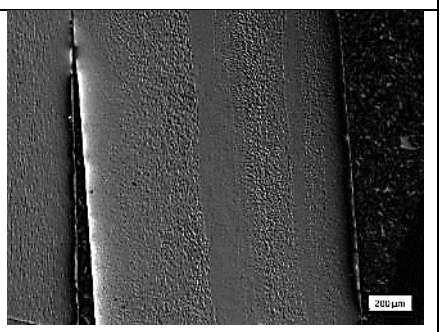
WAAM – HT in air @	**No HT was performed at this temperature in air furnace**		

400 °C			
WAAM – HT in air @ 600 °C	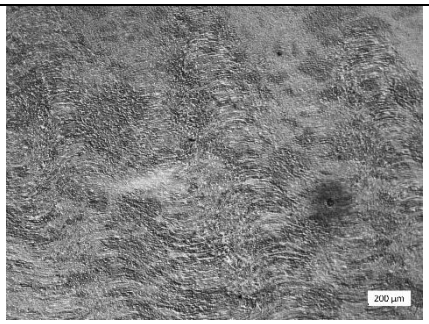	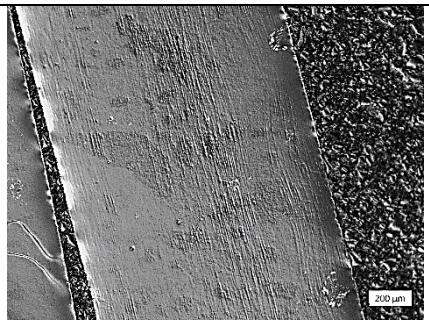	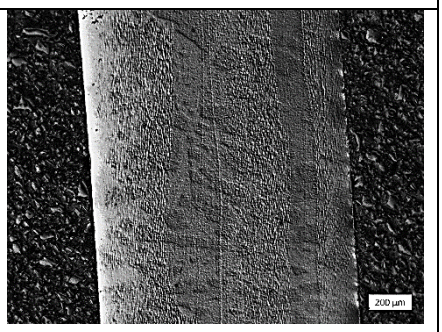
WAAM – HT in air @ 800 °C	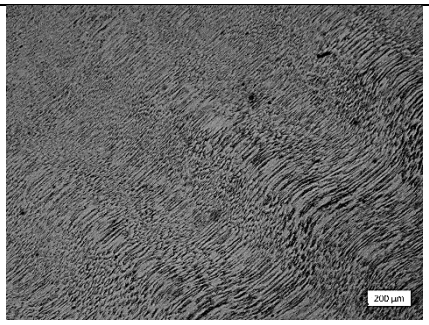	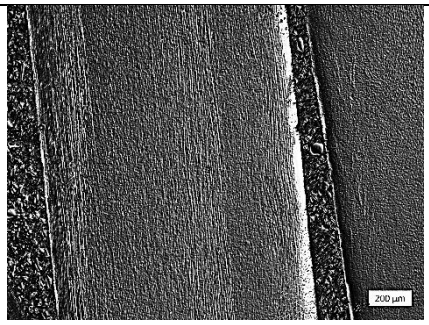	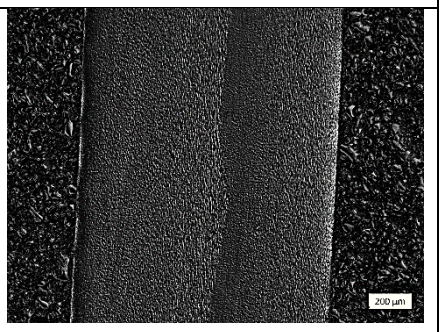

Table A. 2: Microstructure of WAAM material heat treated in air furnace, presented in all three principal directions. All pictures have the same magnification, the white box width is 200 µm.

<u>WAAM material in vacuum furnace</u>

	***R* direction**	***θ* direction**	***Z* direction**
WAAM – No HT	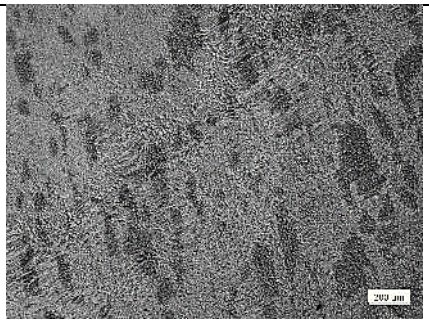	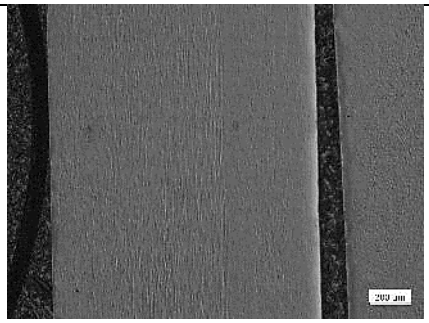	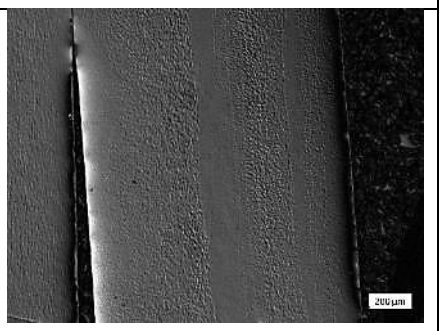
WAAM – HT in vacuum @ 400 °C	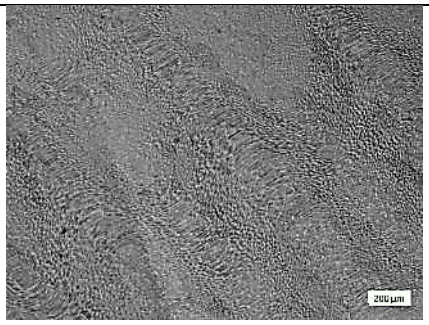	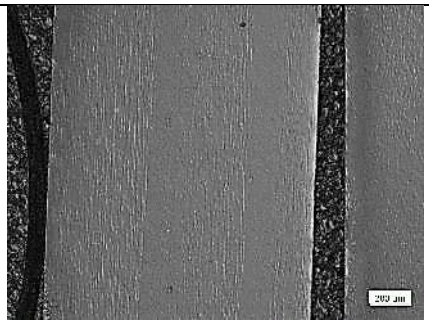	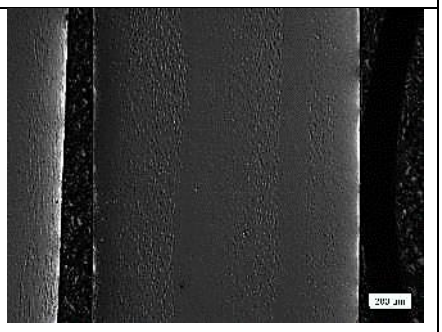

WAAM – HT in vacuum @ 600 °C	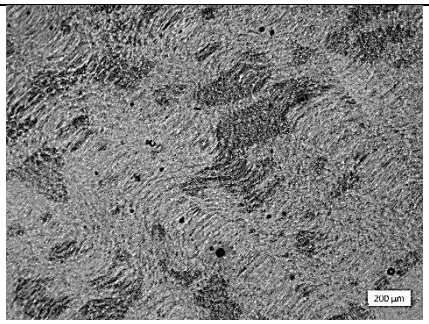	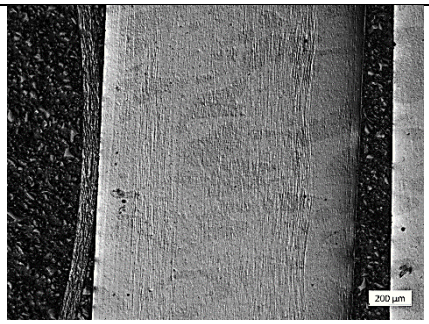	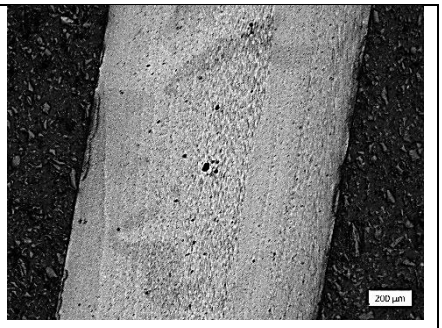
WAAM – HT in vacuum @ 800 °C	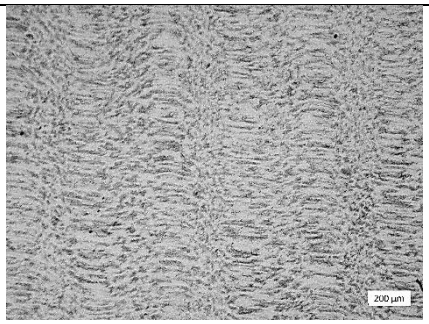	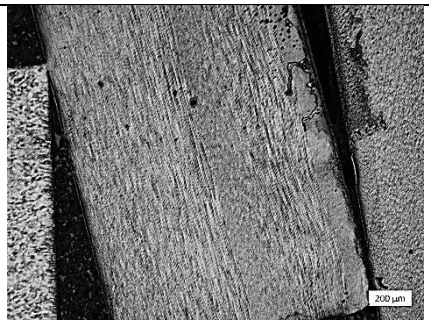	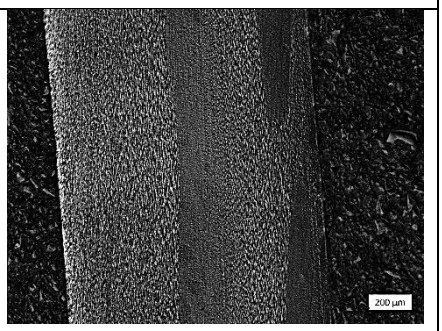

Table A. 3: Microstructure of WAAM material heat treated in vacuum furnace, presented in all three principal directions. All pictures have the same magnification, the white box width is 200 µm.

Acknowledgment

The authors would like to thank Tomer Ron and Maxim Basis for their help with the TEM examination. We wish to thank the anonymous reviewer for pointing out to us the anneal hardening concept.

Funding Sources

This research did not receive any specific grant from funding agencies in the public, commercial, or not-for-profit sectors.

CRediT author statement

Gleb Gil Goviazin: Conceptualization, Methodology, Formal analysis, Investigation, Writing - Original Draft, Visualization.

Daniel Rittel: Methodology, Validation, Writing - Review & Editing, Visualization, Supervision.

Amnon Shirizly: Conceptualization, Methodology, Validation, Resources, Writing - Review & Editing, Visualization, Supervision.

References

[1] G.N. Levy, R. Schindel, J.P. Kruth, Rapid manufacturing and rapid tooling with layer manufacturing (LM) technologies, state of the art future perspectives, CIRP Ann Manuf Technol. 52 (2003) 589–609.

[2] D. Ding, Z. Pan, C. Dominic, H. Li, Process Planning Strategy for Wire and Arc Additive Manufacturing Dong-Hong, 88 (2011) 0–13. https://doi.org/10.1007/978-3-642-19959-2.

[3] S. Chen, H. Gao, Y. Zhang, Q. Wu, Z. Gao, X. Zhou, Review on residual stresses in metal additive manufacturing: formation mechanisms, parameter dependencies, prediction and control approaches, Journal of Materials Research and Technology. 17 (2022) 2950–2974. https://doi.org/10.1016/j.jmrt.2022.02.054.

[4] T.A. Rodrigues, J.D. Escobar, J. Shen, V.R. Duarte, G.G. Ribamar, J.A. Avila, E. Maawad, N. Schell, T.G. Santos, J.P. Oliveira, Effect of heat treatments on 316 stainless steel parts fabricated by wire and arc additive manufacturing: Microstructure and synchrotron X-ray diffraction analysis, Addit Manuf. 48 (2021). https://doi.org/10.1016/j.addma.2021.102428.

[5] A. Hosseinzadeh, A. Radi, J. Richter, T. Wegener, S.V. Sajadifar, T. Niendorf, G.G. Yapici, Severe plastic deformation as a processing tool for strengthening of additive manufactured alloys, J Manuf Process. 68 (2021) 788–795. https://doi.org/10.1016/j.jmapro.2021.05.070.

[6] G.G. Goviazin, A. Shirizly, D. Rittel, Static and dynamic mechanical properties of wire and arc additively manufactured SS316L and ER70S6, Mechanics of Materials. 164 (2021) 104108. https://doi.org/10.1016/j.mechmat.2021.104108.

[7] J. Chen, H. Wei, X. Zhang, Y. Peng, J. Kong, K. Wang, Flow behavior and microstructure evolution during dynamic deformation of 316 L stainless steel fabricated by wire and arc additive manufacturing, Mater Des. 198 (2021). https://doi.org/10.1016/j.matdes.2020.109325.

[8] A. Shirizly, O. Dolev, From Wire to Seamless Flow-Formed Tube: Leveraging the Combination of Wire Arc Additive Manufacturing and Metal Forming, Jom. 71 (2019) 709–717. https://doi.org/10.1007/s11837-018-3200-x.

[9] H. Kolsky, Stress waves in solids., Clarendon Press, Oxford, 1953.

[10] SAE International, Heat Treatment Austenitic Corrosion-Resistant Steel Parts AMS2759/4D, (2018). https://doi.org/https://doi.org/10.4271/AMS2759/4D.

[11] S. Hassan, S. Sharma, B. Kumar, A review of severe plastic deformation, 2017. www.irjes.com.

[12] F. Hamdi, S. Asgari, Evaluation of the role of deformation twinning in work hardening behavior of face-centered-cubic polycrystals, Metall Mater Trans A Phys Metall Mater Sci. 39 (2008) 294–303. https://doi.org/10.1007/s11661-007-9356-6.

[13] A.K. Agrawal, A. Singh, Limitations on the hardness increase in 316L stainless steel under dynamic plastic deformation, Materials Science and Engineering A. 687 (2017) 306–312. https://doi.org/10.1016/j.msea.2017.01.066.

[14] T. Ron, O. Dolev, A. Leon, A. Shirizly, E. Aghion, Effect of phase transformation on stress corrosion behavior of additively manufactured austenitic stainless steel produced by directed energy deposition, Materials. 14 (2021) 1–12. https://doi.org/10.3390/ma14010055.

[15] L. Wang, J. Xue, Q. Wang, Correlation between arc mode, microstructure, and mechanical properties during wire arc additive manufacturing of 316L stainless steel, Materials Science and Engineering A. 751 (2019) 183–190. https://doi.org/10.1016/j.msea.2019.02.078.

[16] S. Gudur, S. Simhambhatla, N. Venkata Reddy, Residual stress reduction in wire arc additively manufactured parts using in-situ electric pulses, Science and Technology of Welding and Joining. (2022) 1–7. https://doi.org/10.1080/13621718.2022.2142396.

[17] J.W. Elmer, G. Gibbs, Mechanical rolling and annealing of wire-arc additively manufactured stainless steel plates, Science and Technology of Welding and Joining. 27 (2022) 14–21. https://doi.org/10.1080/13621718.2021.1996003.

[18] J.W. Elmer, K. Fisher, G. Gibbs, J. Sengthay, D. Urabe, Post-build thermomechanical processing of wire arc additively manufactured stainless steel for improved mechanical properties and reduction of crystallographic texture, Addit Manuf. 50 (2022). https://doi.org/10.1016/j.addma.2021.102573.

[19] Z. Zhou, S. Wang, J. Li, Y. Li, X. Wu, Y. Zhu, Hardening after annealing in nanostructured 316L stainless steel, Nano Materials Science. 2 (2020) 80–82. https://doi.org/10.1016/j.nanoms.2019.12.003.

[20] X.Y. Zhang, Q. Liu, X.L. Wu, A.W. Zhu, Work softening and annealing hardening of deformed nanocrystalline nickel, Appl Phys Lett. 93 (2008). https://doi.org/10.1063/1.3062849.

[21] C. Xia, L. Bu, Q. Zhou, Annealing hardening behaviour of cold rolled Al0.5CoNiCu high-entropy alloy, in: J Phys Conf Ser, Institute of Physics, 2022. https://doi.org/10.1088/1742-6596/2338/1/012050.

[22] J.M. Vitek, H. Warlimont, The Mechanism of Anneal Hardening in Dilute Copper Alloys, Metallurgical Transactions A. 10A (1979).

[23] O. Renk, V. Maier-Kiener, I. Issa, J.H. Li, D. Kiener, R. Pippan, Anneal hardening and elevated temperature strain rate sensitivity of nanostructured metals: Their relation to intergranular dislocation accommodation, Acta Mater. 165 (2019) 409–419. https://doi.org/10.1016/j.actamat.2018.12.002.

[24] T.S. Orlova, N. V. Skiba, A.M. Mavlyutov, M.Y. Murashkin, R.Z. Valiev, M.Y. Gutkin, Hardening by annealing and implementation of high ductility of ultra-fine grained aluminum: Experiment and theory, Reviews on Advanced Materials Science. 57 (2018) 224–240. https://doi.org/10.1515/rams-2018-0068.

[25] A.Y. Volkov, I. V. Kliukin, Improving the mechanical properties of pure magnesium through cold hydrostatic extrusion and low-temperature annealing, Materials Science and Engineering A. 627 (2015) 56–60. https://doi.org/10.1016/j.msea.2014.12.104.

[26] J. Gubicza, Annealing-Induced Hardening in Ultrafine-Grained and Nanocrystalline Materials, Adv Eng Mater. 22 (2020). https://doi.org/10.1002/adem.201900507.

[27] S. Kalpakjian, S.R. Schmid, Manufacturing engineering and technology, Sixth edition, Prentice Hall, 2010.

[28] G.E. Dieter, Mechanical metallurgy, First, McGraw-Hill, 1961.

[29] C.P. Dick, Y.P. Korkolis, Mechanics and full-field deformation study of the Ring Hoop Tension Test, Int J Solids Struct. 51 (2014) 3042–3057. https://doi.org/10.1016/j.ijsolstr.2014.04.023.

[30] Y. Zhao, P. Druzhinin, J. Ivens, D. Vandepitte, S. V. Lomov, Split-disk test with 3D Digital Image Correlation strain measurement for filament wound composites, Compos Struct. 263 (2021). https://doi.org/10.1016/j.compstruct.2021.113686.

[31] W.C. Young, R.G. Budynas, Roark's formulas for stress and strain, 7th ed., McGraw-Hill, New York, 2002.

[32] J.W. Elmer, G. Gibbs, The effect of atmosphere on the composition of wire arc additive manufactured metal components, Science and Technology of Welding and Joining. 24 (2019) 367–374. https://doi.org/10.1080/13621718.2019.1605473.